Science and Engineering Research Council
Rutherford Appleton Laboratory
CHILTON, DIDCOT, OXON, OX11 0QX

RL-82-036

In Vivo Imaging of the Human Thyroid with the Rutherford Positron Camera using ^{124}I

J.E.Bateman et al

May 1982

RL-82-036

In Vivo Imaging of the Human Thyroid with the Rutherford Positron Camera using ^{124}I

J E Bateman, A C Flesher, J F Connolly and R Stephenson
Rutherford Appleton Laboratory, Chilton, Didcot, Oxon

D S Fairweather, A R Bradwell, R Wilkinson
Departments of Immunology and Medicine,
Birmingham University, Birmingham, B15 2TJ

ABSTRACT

The Rutherford Multiwire Proportional Counter (MWPC) positron camera has been applied to the imaging of the human thyroid. 3.7 MBq of cyclotron produced ^{124}I was given orally to seven patients presenting at a thyroid clinic. Positron emission tomography (PET) scans were produced between one and thirty-three hours after ingestion of isotope. All pictures correlated well with clinical findings, ultrasonic examination and standard ^{99m}Tc-pertechnetate thyroid emission scans. The PET scans gave much better definition than the pertechnetate scans but did not provide information on "inactive" thyroid areas as revealed by ultrasonic examination. Spatial resolution was of the order of 7 mm (full width half maximum) in the best case, and satisfactory images were obtained with as little as 0.074 MBq of positron emission in the whole gland.

These results show great promise for the further application of this positron camera for in vivo human imaging.

1. Introduction

In vivo imaging of positron emitting isotopes, utilising the collinear 511 keV annihilation gamma rays to produce a tomogram (PET) has several advantages over a single photon emission tomogram system (ECAT)[1]. The ECAT utilises a rotating, collimated gamma ray detector. This imposes the limitation of producing only axial tomograms, and generally requires a high dose of radioisotope for satisfactory counting rates to be obtained. While for some applications the ECAT may prove to be satisfactory, there is a need for a high resolution, high sensitivity tomographic system, particularly when the total activity available to produce the image is limited, and the image contrast poor. These considerations have led to a continuing interest in the PET which, in one form, employs two static, opposed position sensitive gamma ray detectors which can be used to reconstruct tomograms in any plane parallel to the longitudinal body axis. This configuration we shall refer to as the Positron Camera in order to distinguish it from the axial type of positron emission tomography (Positron Emission Computed Axial Tomography or PECAT). The latter tends to share the limitations of single-photon ECAT (viz low sensitivity, limited spatial resolution and restriction for axial views) so that in the area of clinical research serviced by the PECAT there is continuing interest in the application of the Positron Camera[2]. Early attempts to utilise the high potential sensitivity of two large ($\sim$ 30 cm diameter) opposed detectors in the form of two opposed Anger cameras[3] and in the form of two large hybrid Multiwire Proportional Counters (MWPC)[4,5] did not succeed in producing devices with acceptable performance for clinical research. During the last five years, however, two different positron camera systems have been developed respectively at CERN[6] and at the Rutherford Appleton Laboratory (RAL)[7] based on hybrid MWPC technology. (A

hybrid MWPC structure consists of a metal foil or matrix which absorbs the gamma rays and from which the 'knock-on' fast electrons escape into a conventional MWPC to generate electronic signals.) The aim of these projects has been to generate a practical clinical imaging device both in terms of the detector hardware and the complementary (and equally essential) image processing software.

During the summer of 1981 the RAL positron camera became operational with a complete data taking system, but with very limited image processing software available. Early tests at Hammersmith Hospital in London showed that the most promising initial in vivo sites for study in humans were peripheral limbs where strongly active organs were unlikely to overlie each other, and where scattering and adjacent out-of-field activity was minimal. In this situation one could expect to obtain satisfactory images with the limited image processing available.

At the University of Birmingham, in the Department of Immunology, much effort is currently being devoted to the problem of labelling specific tissue by means of an appropriate antibody tagged with a radioactive marker. The availability of the positron emitting isotope ^{124}I from the Nuffield Cyclotron at Birmingham University, combined with standard protein iodination techniques, offered the opportunity to apply the RAL positron camera to this problem. In such antibody studies the amount of activity concentrated in the site of interest is very low ($\sim$ 0.037 MBq) and the contrast with the surrounding tissue is not high ($\sim$ 2:1). It was therefore hoped that the high sensitivity of the positron camera, its high spatial resolution and its ability to focus on a given plane would enhance the images obtained relative to those obtainable from a conventional gamma camera. One particular site of interest is the parathyroid glands in the neck. Calculation showed that the imaging ability of the system in human

neck sites could be satisfactorily validated by studies of the thyroid gland which would require an administered dose of no more than 3.7 MBq ^{124}I, and which would verify the potential of the positron camera for labelled antibody studies. The thyroid gland is particularly suitable for initial studies because of the high uptake of iodine normally observed and the rapid blood clearance, which can be expected to lead to high contrast images with good definition.

The positron camera was installed at the Queen Elizabeth Hospital, Birmingham, and the data collected during a two week period. Computation of the final images was done partly in situ and partly at RAL.

2. The Rutherford Positron Camera

The present positron camera design was originated at RAL some four years ago as a result of an enquiry from the MRC Cyclotron Unit at Hammersmith Hospital. The design followed on from work done at RAL on hybrid MWPC gamma ray detectors[8]) and was partially funded by the MRC Cyclotron Unit. Figure 1 shows the principle of operation of the positron camera in schematic form. A positron annihilates in the tissue of a patient and the two collinear decay gamma rays (511 keV) exit. If these are intercepted by the two MWPC detectors, the event is recorded in the form of x, y and z coordinates of the two 'simultaneous' interaction points in the two detectors. These coordinates allow a digital computer to calculate the vector joining the two detectors along which the positron emitting nucleus must lie. Unfortunately the position of the source nucleus along the vector is not known so that the location of activity along the axis of the detector system (the z-axis) can only be achieved on a statistical basis resulting from the detection of many thousands of events. This fact leads to the importance of the digital computer incorporated in the positron

camera system and the equally vital image processing software. It is thus convenient to separate the description of the system into two parts: hardware and software.

(i) Experimental hardware

The detector head units determine several very important parameters of the positron camera - viz the efficiency, the spatial resolution and the time resolution. The importance of good spatial resolution is self-evident in an imaging detector and the relevance of the efficiency and the time resolution can be expressed by a figure of merit E^2/T where E is the quantum efficiency of one detector for 511 keV gamma rays and T is the coincidence resolving time of the two detectors. (The only definition of a 'true' event is that the two detectors trigger within a period of time T of each other.) Figure 1 shows how the detectors are constructed by building up a sandwich of some 21 sheets of lead kapton laminate (in which the gamma rays convert to a fast electron) interleaved with 20 planes of 20 μm dia gold-plated tungsten anode wires spaced at 2 mm from each other and the plane spaced at 2.5 mm from the nearest lead kapton cathode plane. The fast electrons knocked out of the lead laminate (which consists of 125 μm thickness of lead on either side of a 75 μm sheet of kapton) ionise the filling gas (isobutane) and generate an electron avalanche in the high electric field near the anode wire. The resulting electrostatic pulse couples to the lead strips on the cathodes (which are mutually orthogonal on either side of an anode plane) and so are brought down onto a pair of mutually orthogonal artificial delay lines from which the coordinates of the event are derived by timing. The anode planes are read out in pairs to permit correction of the parallax error which would arise from the considerable depth (10.4 cm) of each detector. Thus three coordinates x, y and z must be recorded for each event.

Accurate measurement of the quantum efficiency (QE) of the detectors is difficult because of secondary scattering from the frames and within the detector structure. The best estimate from various tests is 6 - 7%. The time resolution of the detectors is determined largely by the wire spacings and is measured to be 52 ns, giving a figure of merit for the detectors of 69 kHz. In theory this is the detector signal rate at which the real data rate is matched by the accidental pile-up rate. However, in reality due to scattering in the patient and out-of-field activity, the practical data taking rate is $\sim$ one tenth of this value[9]).

The spatial resolution of the detectors is indicated by the displays of Figure 2 which show the storage oscilloscope image of two ^{22}Na line sources and a histogram of the x-coordinates of the same data. The fwhm (full width at half maximum) of 6 mm observed is limited partly by the detector structure (ie the width of the anode to cathode spacing) and partly by noise in the electronic circuits.

Figure 3 shows the electronic system required to capture and process the pulses derived from the detector head units. The x and y position signals are commoned onto a single pair of readout delay lines in each detector and accurate timing pulses derived by Constant Fraction Discriminators (CFD). These timing pulses are converted into voltage pulses by Time to Amplitude Converters (TAC) for use in an analogue computer which gives a real time display of a chosen reconstruction plane within the patient on a storage oscilloscope (Tx 611). In parallel, Time to Digital Converters (TDC) generate binary numbers proportional to the x and y coordinates of the gamma ray event for transmission to the computer via the CAMAC bus. A further box encodes the anode planes triggered in the two detectors and transmits them to the two readout systems. None of the above data transfers take place unless the basic criterion of a 'good' event is met,

viz a fast coincidence (within 52 ns) of any anode plane of detector 1 with any anode plane of detector 2. The circuitry for this is shown in the top left corner of Figure 3.

In digital data taking, the computer transfers the two 3-vectors from the CAMAC into a 511 event buffer in memory and then transfers a full buffer either to the RL-01 rigid disk or the magnetic tape drive (Figure 3). An event is stored in 5 bytes, so a typical data exposure of 10^5 events requires 0.5 Mbyte of permanent storage medium. The data taking rate capability of this set-up is not very fast, simply due to hardware limitations, but with a maximum transfer rate of $\sim$ 1 kHz to tape and 2 kHz to disk, it proved adequate for the data rates obtained in the present study. A FORTRAN program controlled the details of data taking producing a print out of important parameters such as total counts, mean rates, accidental counts, etc.

The analogue computer and storage oscilloscope display performed an essential function in giving a real time display which permitted the accurate positioning of patients before digital data taking commenced.

(ii) Digital Image Processing and Display

The computer hardware supporting the software effort is indicated in Figure 3. In addition to a DEC LSI 11-23 with the full 128K words of memory and fast floating point arithmetic card, we have a 5 Mbyte RL-01 rigid disk for program development and fast back-up store for production programs (occasionally the disk was used for fast data taking), an RX-02 dual floppy disk drive for storage of the picture files produced by the analysis programs and an EMI 8800 series, 45 inches/second, tape drive for bulk raw data storage and system back-up. The final images were displayed through a

Sigma Electronics Graphics Output Controller on a TV monitor in 16 levels of grey or colour or as line printer coded intensity plots of 128 pixels x 128 pixels, each pixel being 2.3 mm x 2.3 mm.

The first stage of data processing consists of the calibration of x and y TDC numbers into coordinates in the range 1 - 128 corresponding to the 300 mm aperture of the two detectors, and the correction of the parallax error induced by the detector thickness using the stored z coordinate. The basic raw images were then formed by histogramming the intersections of the positron decay vectors with a number of planes (normally 5) parallel to the detector planes and spaced at locations in the middle of the detector space chosen by the operator to correspond to sites of interest within the patient. During this process a limit is put on the possible angle[10]) that rays can make with the z axis (normal to the detector planes) so that, at a cost of $\sim$ 60% of detected events we ensure an approximately uniform detection efficiency over a sensitive volume of 15 cm x 15 cm x 15 cm in the centre of the detector system. Any organ of interest must be located within this volume.

The raw reconstruction pictures generally exhibit low contrast and high statistical noise (the highest pixel counts rarely exceed $\sim$ 100 in the images presented in this report). The next stage of processing is thus the deconvolution of the system point response function and the filtering out of high frequency statistical noise. Compton scattered events and accidental fast coincidence events degrade the point response function of the system. However, early work showed that these two effects generate principally long range tails in the point response function (see Figure 2) which are approximately constant in shape and which, with care, can be modelled accurately enough for our purposes. The basic point response function is measured by putting a 0.37 MBq point source of ^{22}Na in the

midfield with the appropriate portion of a human being to generate the scatter situation which it is required to model. The deconvolution process is done by fourier transforming (FT) the raw images, dividing this FT by the stored FT of the point response function and back transforming after applying a roll-off filter in frequency space. The 50% frequency of the roll-off function is chosen empirically by inspection of the resulting image since the optimum value is a function not only of the pixel statistics in the image but also the contrast. In general it has been found by experiment that in the present imaging situation cut off values (CT) of between 10 and 15 (expressed as harmonics of the 300 mm field) are used depending as the pixel statistics vary between 50 and 150. Figure 4 shows an example of an image of a normal thyroid which is showing very low uptake of ^{124}I (due to a recent attack of thyroiditis) and so giving only 20,000 events in the picture. However, the initial assumption (Figure 4a) that the image would become unstable due to low statistics with a cut-off greater than 10 was found to be invalid because of the highly nodular concentration and high contrast. Figure 4c (CT = 15) actually is showing about the physical resolution of the positron camera ($\sim$ 7 mm fwhm) with a negligible background and the thyroid structure showing stable contours. One notes the very good separation of the two lobes at the isthmus. If the contrast and the pixel statistics are poor one cannot make use of physical resolution of the detectors. The lower filter cut off values correspond to spatial resolutions of approximately 8 - 9 mm fwhm (CT = 12) and 12 - 14 mm fwhm (CT = 10). With present software the deconvolution process takes approximately 6 minutes per picture.

Given the high contrast source presented by the human thyroid (particularly at 24 h after ingestion) and its limited spatial extent, it was felt that the next, more complex, step of a full attempt at a 3 dimensional reconstruction would not significantly enhance the images obtained with the

positron camera in the context of this study. Consequently, the images presented have no more processing than is described above. Work is currently in hand on software for situations in which the depth of information is vital to the interpretation of the images.

In order to meet the requirements of being close to both patients and a cyclotron the entire positron camera system including detectors, gas supplies, electronics and computer was built into a lightweight transport container capable of being transported on a standard road trailer. A view of the inside of the container is shown in Figure 5.

In practice the positron camera was operated with a detector separation of between 45 cm and 60 cm, the larger figure being necessary to accommodate a 50 mm lead shield around each detector (except for the active aperture, of course). This shield is essential if the positron emitting activity is disseminated throughout the patient in order to cut down on uncorrelated trigger events which generate accidental coincidences. At 60 cm separation the sensitivity of the system is 351 Hz/MBq of positron emitter with the data taking system capable of handling a maximum of about 3.7 MBq in the field of view. (At 45 cm separation the sensitivity is approximately double the above figure.)

3. Isotope Preparation

^{124}I was produced by 40 MeV alpha particle bombardment of natural antimony in the Nuffield cyclotron at Birmingham University. Aluminium targets flame-sprayed with antimony were kindly supplied by Dr H Sharma of Manchester University who also milled the active face after irradiation. The millings were treated with hot 6M NaOH to dissolve the aluminium and the residue washed to remove traces of hydroxide. Distillation of the ^{124}I

activity from the antimony residue was as previously described[11]), but without the use of added carrier iodine. The final product was diluted in sterile saline BP containing a trace of sodium thiosulphate. The overall yield was less than 10% of the ^{124}I activity on target at the time of milling. Isotopic purity was checked by gamma ray spectrum analysis using a Ge(Li) spectrometer. ^{125}I activity was checked by allowing the product to decay and estimating the residual ^{125}I activity. At the time of use these tests indicated no positron emitter other than ^{124}I and the contamination with all other isotopes was less than 0.1%. No long lived isotope other than ^{125}I was detected.

4. Dosimetry

Radiation to the thyroid itself is the limiting factor when using Iodine isotopes[12]). A dose of ^{124}I was chosen to give an absorbed dose equivalent to that following the usual dose of ^{131}I for a thyroid scan (1.8 to 7.4 MBq). Using a standard model calculation shows that for each Bq administered, ^{124}I would produce about 70% of the absorbed dose from ^{131}I[13]). Thus the doses used meet this criteria.

5. Patients and Results

Seven patients presenting to the thyroid clinic of the Birmingham General Hospital were investigated after giving their informed consent. Clinical details are given in Table 1. Female patients were past the menopause. All were taking a diet containing normal amounts of stable iodine, and none were taking any drugs at the time of study except patient 2 who was receiving polychemotherapy for Hodgkins' disease. All were clinically and biochemically euthyroid. The isotope was administered orally except in Case 2 when it was given by intravenous injection. PET scans were obtained between 1 and 36 hours after administration of ^{124}I.

Details of the patients' PET scans are listed individually with the supporting investigations for comparison. Table 1 summarises details of PET scans.

Patient 1. Female. Aged 56

Diagnosis - Multinodular goitre.

Ultrasound - Cystic lesion right with area of increased ultrasonic reflectivity suggestive of fibrosis. Large cystic mass on left.

PET (24h) - Rim of activity in upper left lobe. Most of left lobe non-functional. Right at least two cystic areas - see Figure 6.

Patient 2. Male. Aged 72

Diagnosis - Normal thyroid (IV dose). (Hodgkins' disease with nodes in neck).

PET (20h) - Salivary uptake and uniform thyroid emission. See Figure 7.

Patient 3. Male. Aged 38

Diagnosis - Multinodular goitre.

Ultrasound - Left side cystic.

$^{99m}TcO_4^-$ scan - Left side cold.

PET (1, 6 and 24h) - Show gradually increasing ^{124}I uptake into three discrete active areas. These represent only a small fraction of the gland. The pathology of such multinodular lesions shows focal areas of active thyroid tissue among inactive thyroid cells, fibrous areas and cysts, see Figures 8 and 9.

Patient 4. Female. Aged 68

Diagnosis - Multinodular goitre.

Ultrasound - Uniform enlargement with retrosternal extension on right.

PET (26h) - Reduced activity on left lobe. Small area of increased activity anterio/lateral to the right lobe. Retrosternal extension on right. See Figure 10.

Patent 5. Female. Aged 54

Diagnosis - Thyroiditis.

Ultrasound - Normal.

$^{99m}TcO_4^-$ scan - Virtually no uptake detected.

PET (24h) - Shows a normal sized gland as with patient 2. The activity is not uniform in the gland, there being two main areas of activity less than 15 mm diameter. The isthmus shows in the anterior view and two small areas of activity just outside the smooth outline of the lobes. See Figure 11.

Patient 6. Female. Aged 55

Diagnosis - Multinodular goitre.

Ultrasound - Marked enlargement of the right lobe and isthmus. Slight enlargement of left lobe.

$^{99m}TcO_4^-$ scan - Uptake only on right side.

PET (4h and 33h) - Big right lobe, slight activity in isthmus and a hot spot in the later scan posteriorly. See Figure 12.

Patient 7. Male. Aged 60

Diagnosis - Multinodular goitre.

Ultrasound - Enlargement of whole gland with retrosternal extension and cystsic degeneration on the right.

$^{99m}TcO_4^-$ scan - Normal right lobe. Asymmetric left lobe with reduced activity in the lower portion suggestive of a retrosternal mass.

PET (25h) - Similar to the $^{99m}TcO_4^-$ scan. See Figure 13.

6. Comments on the PET Images

Before discussing in detail the images produced by the PET system, it is important to take account of the techniques and conventions used in the display of the data which resides (in its final form) as an array of 16,000 numbers (128 x 128) on a floppy disk. The simplest display, and therefore in a sense the most truthful, is obtained by coding these numbers in a line-printer print-out. The contour plots in Figures 6 - 13 are made from such line-printer outputs and have the advantage of showing the actual relative numerical values of the pixel contents. Contouring has been done at 75%, 50%, 25% and 10% of the peak value with an extra contour used when a distinctive feature of the image happens to lie midway between the standard values. The calibration square of 10 pixels x 10 pixels (1 pixel is 2.34 mm wide) shows the scale and the slight distortion of the x scale relative to the y scale caused by the line printer spacing. On these prints (which are approximately actual size as they are produced) the clavicles have been sketched from the chest X-ray along with the outlines (dotted) of any obvious lesions.

The video image display system (via the Graphics Output Controller (GOC) and a TV monitor) is the most convenient display medium but considerable

care must be exercised if the data is not to be misinterpreted. The problem derives from the exponential brightness versus grid voltage characteristic of a TV tube. In order to compensate for this we take the natural logarithm of our pixel numbers before sending them to the GOC. This over-compensates for the TV tube characteristic, but when the screen is photographed by a camera containing polaroid film, the superlinear film characteristic corrects back again to give an approximately linear brightness versus pixel count response. The TV images shown in Figure 4 and 6 - 14 have all been treated this way unless annotated with the word 'linear' indicating that logarithms have not been taken. In this case the highlights of the image are presented differentially to one's attention. This technique is useful when searching for small differences between images (when for example objects are going in and out of focus through the planes).

The quality of any particular image is determined by three principal factors: (i) the physical spatial resolution of the system (ie the response of the system to a point source with infinite statistics), (ii) the contrast in the target object distribution, and (iii) the pixel statistics. The interaction between these thre parameters is complex, but several 'limiting' statements can be made which can be demonstrated with our images.

1. Good 'physical' spatial resolution is always desirable but in the absence of good pixel statistics (dependent on the detector sensitivity) and reasonable contrast, it can rapidly become of merely academic interest since at the higher spatial frequencies statistical noise will dominate. As will be seen from Table 1, the cut off frequency on our low pass filter must often be set to give lower spatial resolution than the 'physical' resolution of the system (corresponding to CT $\sim$ 15) due to poor contrast and statistics.

2. Poor contrast in the target distribution demands very good statistics for imaging and a high contrast object (10:1 say) can be imaged with remarkably low statistics - see for example Figure 4 where total counting statistics of a mere 20,000 are capable of giving an excellent image at full spatial resolution because of the complete blood clearance and high localisation of the ^{124}I. In Figure 7 one sees on the other hand a background level of $\sim$ 15% due to poor blood clearance with only a very small uptake in the field of view ($\sim$ 8%) and only approximately one-third of that in the thyroid. The value of the tomographic capability of the system is shown in Figure 7 where (a) shows the reconstruction in a forward plane (6 cm anterior to the best thyroid image) in which salivary uptake shows clearly with an out-of-focus thyroid. The salivary has, however, disappeared in plane 5 where the focussing property of the positron camera acts in such a way as to enhance the contrast of the thyroid relative to the general blood pool signal. It is this ability of the positron camera to enhance the contrast in the region of interest which is probably its most important asset.

3. Pixel statistics are determined by the amount and distribution of positron emitting isotope inside the target object and by the sensitivity of the detector system. The two former parameters also determine the radiation dose to the organ concerned and so are subject to firm limits. The high local dose from the stopping positron and the fact that only 23% of the total emission of ^{124}I is in the form of positrons makes the situation less than ideal for the positron camera resulting in exposure times of 10 - 20 minutes for most of the images presented (see Table 1). Since the system sensitivity depends on the quantum efficiency of the detectors (QE) squared, it is expected that the next stage of development will result in an increase of sensitivity of a factor of 2 - 3, bringing scan times down correspondingly. There is an optimal size of lesion which

any statistics limited system can image, namely about the same size as the 'physical' resolution of the system, ie in our case $\sim$ 7 mm diameter. An object of this size produces the brightest image possible for the total counts within it and also exhibits the strongest focussing effect through the tomographic planes with a resolution of $\sim$ 3 cm fwhm in depth (z). This dimension correlates well with the expected diameter of antibody labelled parathyroid glands.

Information about the depth of active sites in the neck of patient 3 is obtained from the tomographic slices in Figure 8. Between planes 3 and 5 (separated by 2 cm) one sees the appearance of another active node (compare Figure 8a and 8d). The use of the 'linear' display in highlighting the active nodes is shown in Figure 8e which shows the same data as that of Figure 8d in this display mode. This display mode is also used in Figure 9 to show the concentration of ^{124}I in the two main active nodes of the thyroid of patient 3. The accompanying contour maps show the decreasing areas contained by the 75% contour as time progresses.

In the normal thyroid shown in Figure 11 the ^{124}I image shows a much cleaner picture than that given by the pertechnetate, with no residual salivary activity. This is probably due to the high specificity of iodine for the thyroid and the 24h blood clearance time given in this case.

A further example of the control of the spatial resolution by means of the filter cut off frequency is shown in Figure 12. The optimal focal plane for the thyroid of patient 6 is shown with CT = 15 (Figure 12a, b) and CT = 10 (Figure 12c, d). The apparently uniform left lobe in the CT = 10 image, breaks up into nodules in the higher resolution scan but the amplitude of the background noise oscillations also increases as shown by the contour plots. The image presented by Figure 12a, b is statistically valid but any

attempt at higher spatial resolution would bring the danger of confusing artifacts. In every image there is a judgement to be made about the value of CT. Since this is a complex question involving (as discussed above) different parameters and with different effects on different parts of the image, the best value is selected by trial and error.

7. Conclusions

The above data show the ability of the RAL positron camera to image small sites containing less than 0.1 MBq of ^{124}I. At the same time a production route for ^{124}I has been established. Calculation shows that a lesion (Figure 11a) containing 0.074 MBq in one cm^2 gave 2,000 counts. On the same basis, but assuming an image contrast of 2:1, one would expect 0.0074 MBq in 1 cm^2 to give 200 counts on a background of 100. With suitable filtering the image contrast might be enhanced three fold (100 counts on $\pm$ 17 counts of background). This compares very favourably with current two dimentional localisation using a gamma camera. Thus the main object of the study has been achieved; mainly to demonstrate that the present camera is suitable for application to radio-immunolocalisation in the neck.

Further developments include the use of ^{124}I labelled antibodies (two such patients have already been studied) and the improvement of depth resolution. For the latter we are employing a more sophisticated software kit which makes use of multiple views of the patient.

In the longer term, a development program on the camera hardware is presently in hand aimed at improving the field of view, spatial resolution and sensitivity by a factor of two or more. This will enable the camera to be used in any area of the body.

The present in vivo study has supported previous claims of the performance of the RAL positron camera[7]) and gives considerable impetus to pursue in vivo localisation of human tissues.

Acknowledgements

In addition to those named in the text, we would like to express our thanks to the following colleagues for their assistance in the course of the project: at RAL, Mr P Mackay and Mr R J Apsimon, at the Physics Department of Birmingham University, Dr M Scott and at the Nuffield Cyclotron, Birmingham, Mr S Downey, Mr E Cartwright and Mr F Stuart. The clinical study would not have been possible without the help and encouragement of Dr P W Dykes of the Birmingham General Hospital.

References

1. G L Brownell, T F Budinger, P C Lauterbaur, P L McGeer. Positron Tomography and Nuclear Magnetic Resonance Imaging. Science 1982; 215: 619-626.
2. T Jones. British Medical Bulletin (1980), 36, pp 231-236.
3. G Muehllehner, M P Buchin and J H Dudek. IEE Trans. Nucl. Sci. NS-23 (1) (1976) 528.
4. R A Reynolds, R E Snyder and T R Overton. Phys. Med. Biol. 1975, 20, 136.
5. R S Hattner, C B Lim, S J Swann, L Kaufman, V Perez Mendez, D Chu, J P Huberty, D C Price and C B Wilson. IEEE Trans. Nucl. Sci. NS-23 No 1, 523 (1976).

   V Perez Mendez, C B Lim, D Ortendahl, R Semper, A Cheng, D Chu, R Hattner, L Kaufman and D C Price. Nucl. Insts. and Meth. 156 (1978) 33.
6. A P Jeavons. Nucl. Instr. and Meth. 156 (1978) 41.

   A P Jeavons. 5th Int. Conf. on Positron Annihilation, Lake Yamanaka, Japan (1979).

   A P Jeavons, K Kull, B Lindberg, G Lee, D Townsend, P Frey and A Donath. Nucl. Insts. and Meth. 176 (1980) 89.
7. J E Bateman, J F Connolly, R Stephenson and A C Flesher. Nucl. Insts. and Meth. 176 (1980) 83.
8. J E Bateman and J F Connolly. Phys. Med. Biol. 23, (1978) 455.
9. J E Bateman. Rutherford Laboratory Report RL-78-006.
10. D Townsend, C Piney and A P Jeavons. Phys. Med. Biol. 23 (1978) 235.
11. D J Silvester, J Sugden, I A Watson. Preparation of Iodine-123 by - particle Bombardment of natural antimony. Radiochemical Radioanalytical Letters 1969; 2 : 17-20.
12. J Vennart, M Minski. Radiation Doses from Administered Radio-Nuclides. Brit. J Radiology 1962; 35 : 372-387.

13. E W Emery, J F Fowler. Radiation Dosimetry in Diagnostic Procedures in Eds N H Belcher and H Vetter. Radioisotopes in Medical Diagnosis, Butterworths London 1971.

Figure Captions

Figure 1 Schematic diagram of the mode of operation of the positron camera showing the detector structure of multiple lead foil - MWPC sections. The upper bubble indicates the nature of the gamma conversion and detection process.

Figure 2 (a) This shows the analog computer - storage oscilloscope image generated by two positron emitting line sources (^{22}Na) each 50 mm long, spaced 50 mm apart, placed in the central plane of the positron camera field.

(b) This presents a histogram of the coordinates of the dots on the oscilloscope image, permitting a measurement of the line width response function (6 mm fwhm).

Figure 3 This diagram is a general schematic of the positron camera electronics and the computer system which controls the data taking and processes the final images. Not shown is the detailed electronic logic which selects valid events and also the computer's line printer output channel.

Figure 4 In this figure we see the effect of changing the cut-off frequency of the low frequency pass filter during the image processing. The 50% frequency of the filter (CT) is varied from 10, (a) through 12, (b) to 15 (c). The frequency is measured in harmonics of the 30 cm field so that these frequencies have values of 0.33, 0.4 and 0.5 in units of cm^{-1}. The data comes from a ^{124}I labelled normal thyroid, which, as the spatial resolution is increased, is shown to have, in fact, quite strong nodes. The original data set comprised 20,000 events.

Figure 5 This photograph of the interior of the positron camera container shows most of the essential elements of the system: the detectors and patient couch, the control electronics and the tv monitor, the LSI-11/23 computer and its peripherals.

Figure 6 Here we see the standard tv monitor display of the ^{124}I distribution observed in the thyroid gland of patient 1 (a), and the contour map of the activity distribution as plotted out on the line printer (b). The tv image is scaled in 16 grey scales normalised to the highest pixel and the line printer output is scaled in 32 characters with contours drawn at 75%, 50%, 25% and 10% of the peak value (other contours are occasionally inserted if it seems useful). The original line printer image is almost exactly to actual scale (with a slight mis-match between the axes due to the printer spacing) so that anatomical details (such as the clavicles) can be traced over with indications of calcification (dotted lines) from the chest X-ray. The calibration square is 23.4 mm on side. The reconstruction produces 5 planes from which the plane showing the 'best focused' image is generally presented. The patient is always seen in the anterior view.

Details of the statistics and ^{124}I dose are given in Table 1.

The above general remarks apply to Figures 7 - 13 with any exceptions noted below.

Figure 7 Here we see an example of depth resolution in the data from patient 2 with the most anterior plane (No 1) showing the salivary uptake (a) and an out-of-focus thyroid gland, and the most posterior plane (No 5) (6 cm further back) showing no salivary

and a focused normal thyroid gland (b) and (c). Also noticeable is the statistical interference from the high residual blood pool which produces modulation at the 20% level in the contour plot.

Figure 8 This figure shows the ^{124}I images taken at 24h after ingestion in a patient (No 3) with a massive goitre. The uptake of ^{124}I is very nodal. The strongest nodes appear in all planes but the weaker ones reveal their depth by appearing best in different planes. Thus a small node bottom centre appears better in plane 5 (d) than in plane 3 (a). The 'linear' display of plane 5 (e) shows the 'hotter' parts of the picture with a clearer indication of the location of the active nodes. The contour plot of plane 3 is also given (c) and the pertechnetate scan of this patient for comparison (b).

Figure 9 The long half-life (4.2 days) of ^{124}I permitted a sequential study on patient 3 who was scanned at 1h (a), 6h (b) and 24h (c). The progressive concentration of the ^{124}I in the active nodes is clearly shown in the contour plots and the 'linear' tv display shows even more dramatically the concentration of the activity as time progresses.

Figure 10 This shows the PET scan for patient 4 (b) and (c) with the pertechnetate scan for comparison.

Figure 11 This shows the high resolution PET image obtained from a normal thyroid exhibiting low uptake (patient 5). The PET scans (reconstruction plane 2) in Figures (a) and (b) show higher contrast and resolution relative to the pertechnetate scan (c).

Figure 12 This PET image from patient 6 is used to show the trade-off between spatial resolution in the final image and statistical noise induced artefacts. Figures (a) and (b) show the thyroid image with CT = 15 and (c) and (d) with CT = 10. The nodularity of the uptake in the gland exhibited by (a) and (b) is clearly real but equally the background oscillations have risen from 7% to 10%.

Figure 13 This shows the PET scan (a) and (b) for patient 7 with the pertechnetate scan for comparison (c).

Table 1

PATIENT DIAGNOSIS	DOSE OF ^{124}I ADMINISTERED (MBq) ROUTE	MEASURED ^{124}I UPTAKE AT SCAN TIME	TOTAL COUNTS IN IMAGE (x 10^5)	EXPOSURE TIME (MINS)	CENTRAL PLANE PLANE SEPARATION (cm)	FILTER CUT OFF (SPATIAL FREQUENCY)
1. Female 56 yr Multinodular goitre	7.4 orally	33.0% at 24h	2.05	20	24.6 1.0	15
2. Male 72 yr Normal thyroid	3.7 I.V.	8.2% at 20h	0.41	61.6	20.7 1.5	12
3. Male 38 yr Multinodular goitre	3.7 orally	20.8% at 1h	0.41	21.5	23.4 0.8	10
"	"	31.0% at 6.5h	0.82	28.2	27.2 2.0	10
"	"	38.9% at 24h	0.82	28.0	30.0 1.0	10
4. Female 68 yr Multinodular goitre	3.7 orally	35.3% at 26h	0.41	12.0	25.0 1.0	10
"	"	35.0% at 26h	0.31	9.5	29.0 1.0	10
5. Female 54 yr Thyroiditis	3.7 orally	7.6% at 24h	0.20	19.0	30.6 2.0	10,12,15
6. Female 55 yr Multinodular goitre	3.7 orally	17.4% at 4h	0.51	23.5	26.5 1.0	10
"	"	25.2% at 33h	0.31	12.2	27.2 1.0	10,15
"	"	25.2% at 33h	0.31	12.2	27.2 1.0	10,15
7. Male 60 yr Multinodular goitre	3.7 orally	27.1 at 25h	0.72	32.0	25.3 2.0	10

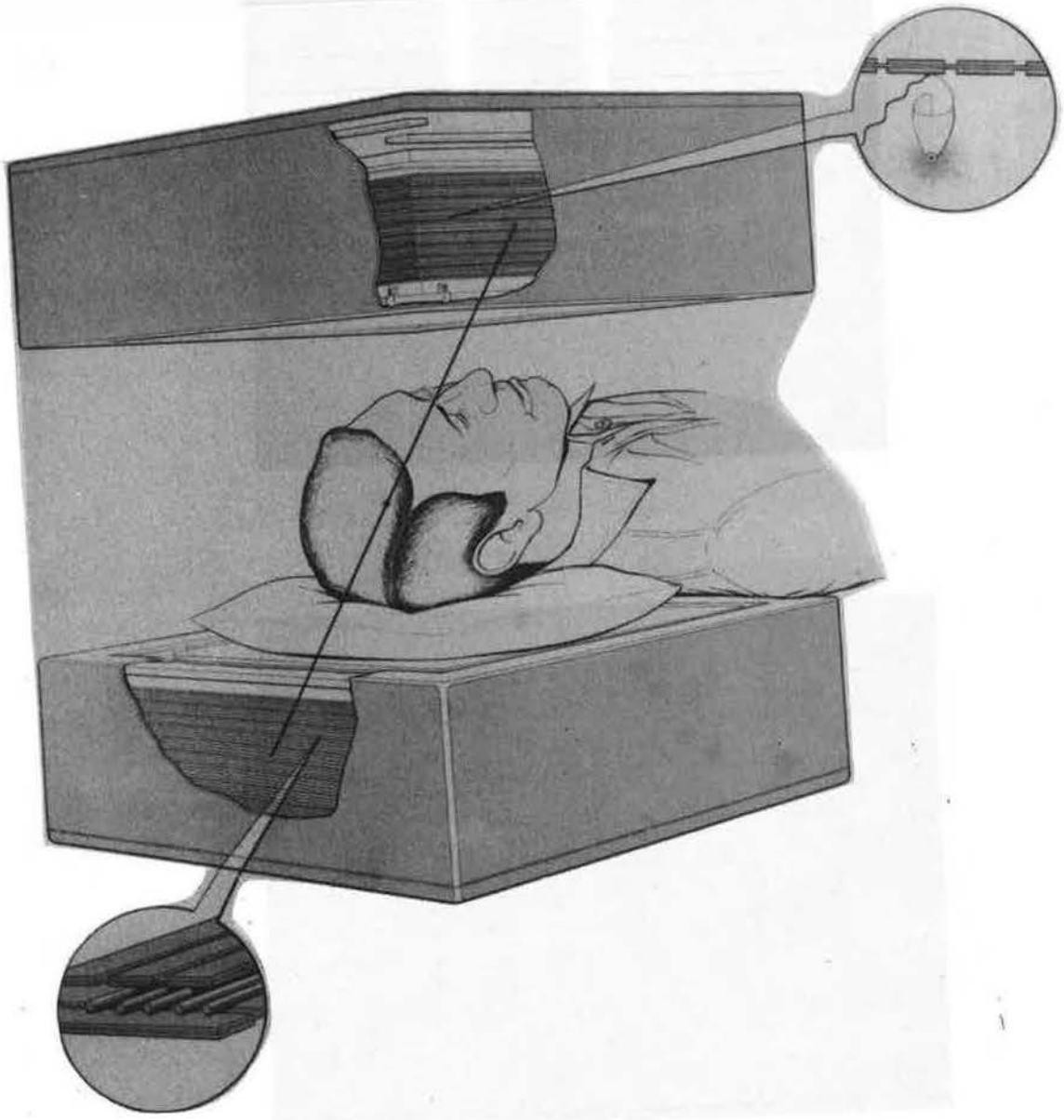

Figure 1

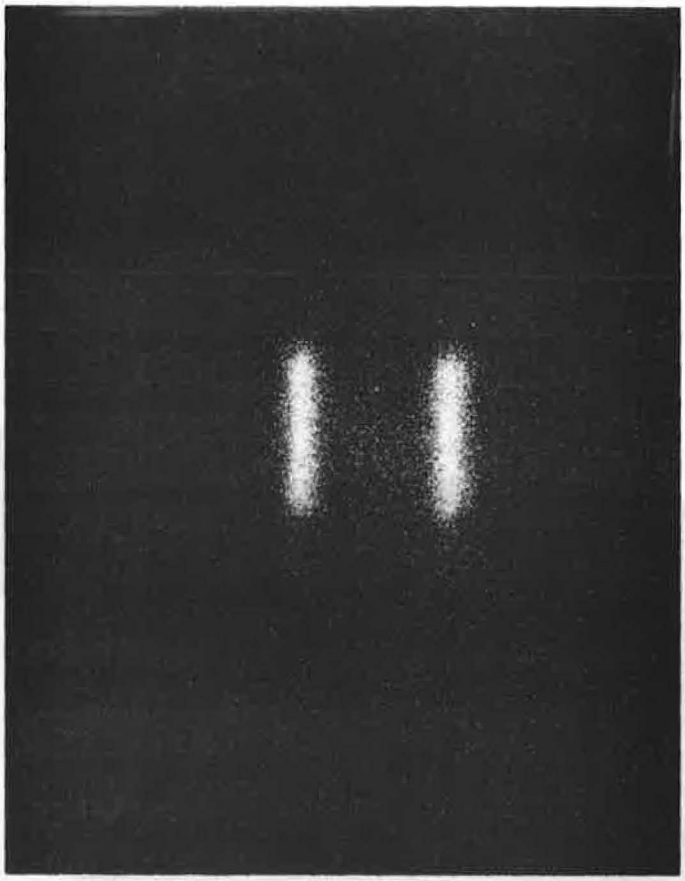

(a)

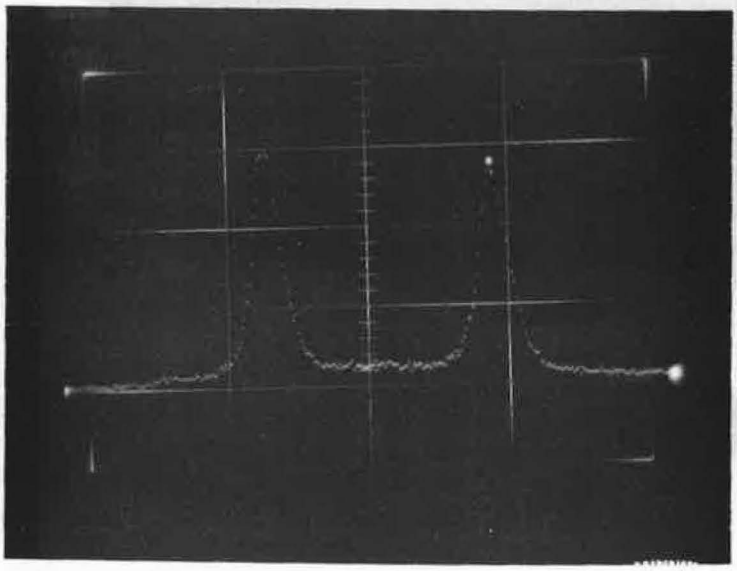

(b)

Figure 2

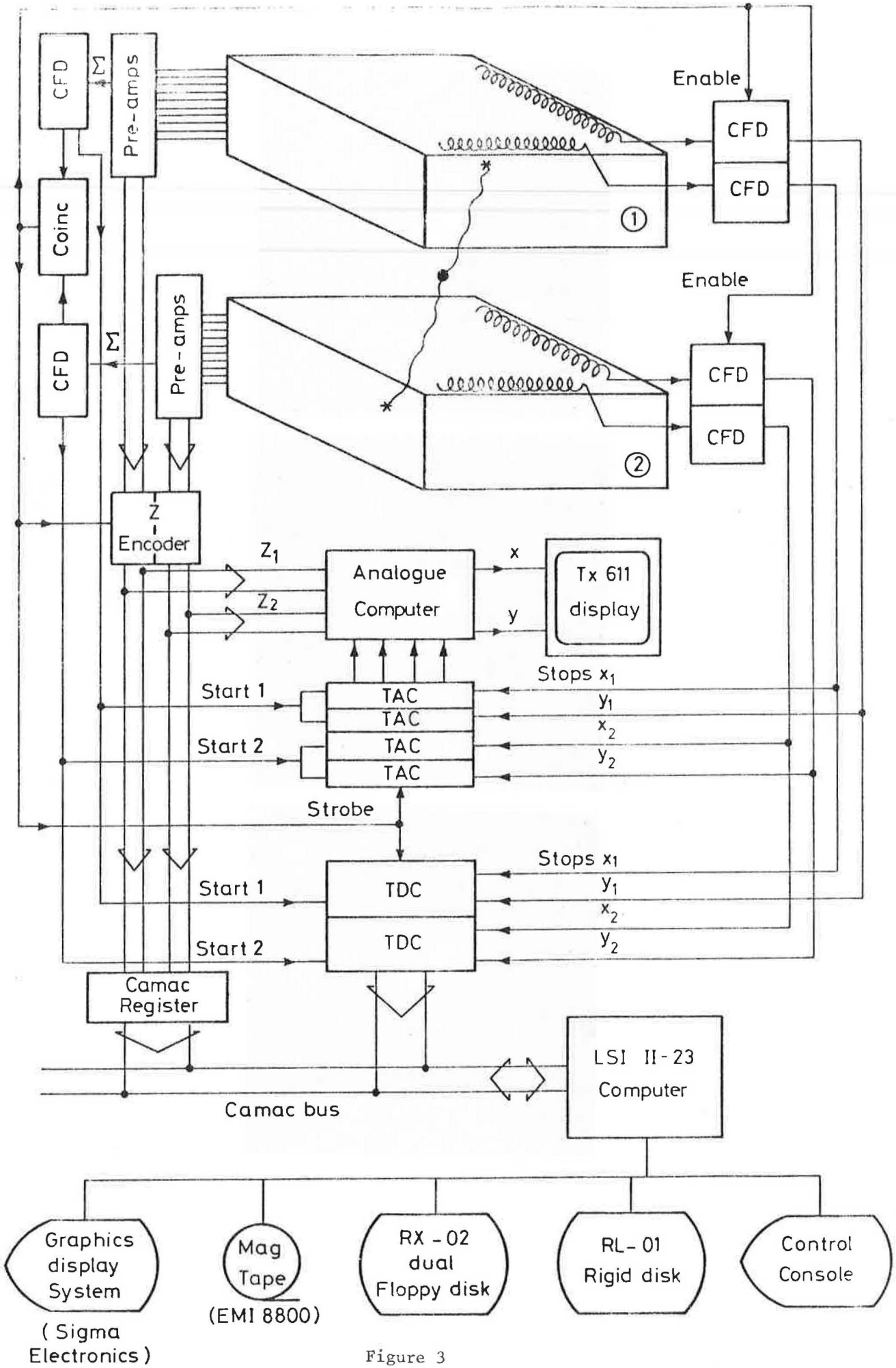
CFD
Σ
Pre-amps
Coinc
CFD
Σ
Pre-amps
Enable
CFD
CFD
①
Enable
CFD
CFD
②
Z
Encoder
Z_1
Z_2
Analogue
Computer
x
y
Tx 611
display
Start 1
Start 2
TAC
TAC
TAC
TAC
Stops x_1
y_1
x_2
y_2
Strobe
Start 1
Start 2
TDC
TDC
Stops x_1
y_1
x_2
y_2
Camac
Register
Camac bus
LSI II-23
Computer
Graphics
display
System
(Sigma
Electronics)
Mag
Tape
(EMI 8800)
RX-02
dual
Floppy disk
RL-01
Rigid disk
Control
Console

Figure 3

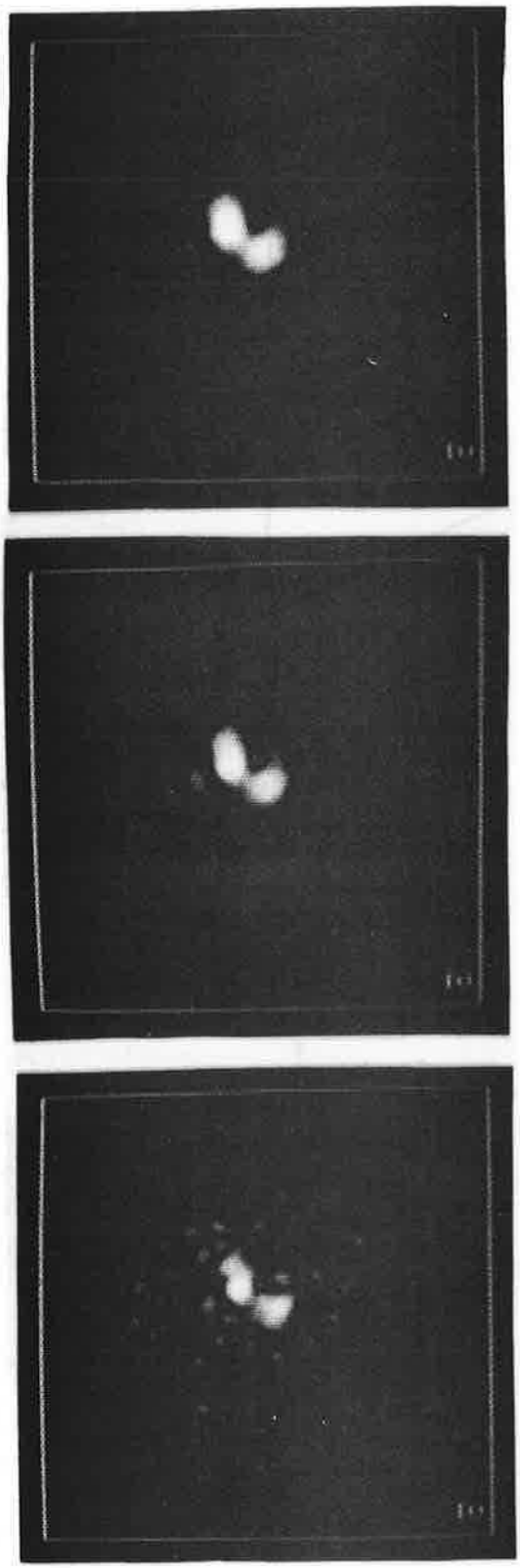

(a)

(b)

(c)

Figure 4

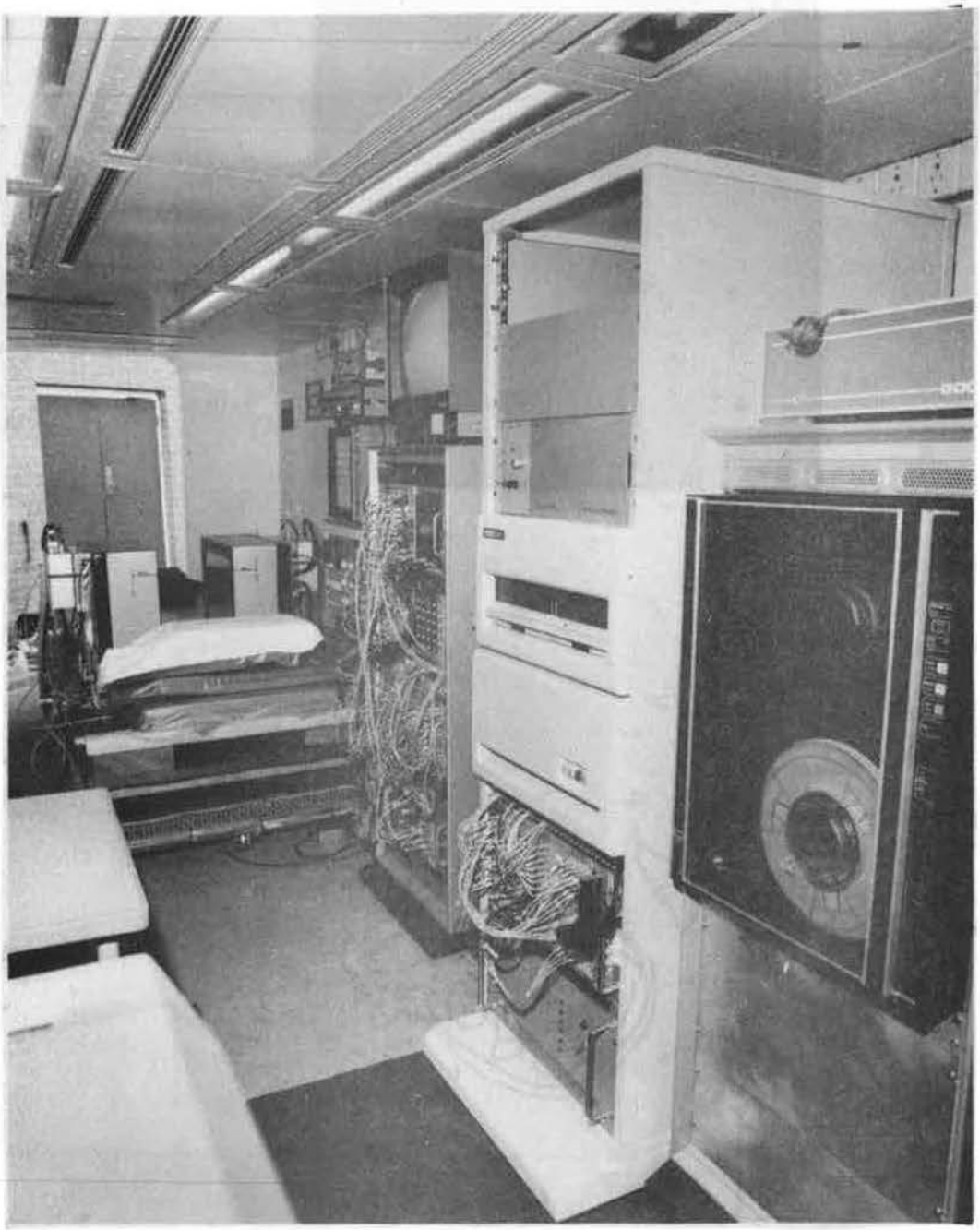

Figure 5

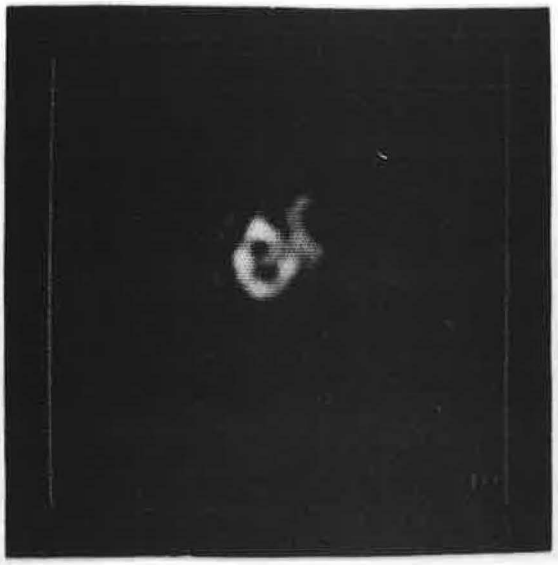

(a)

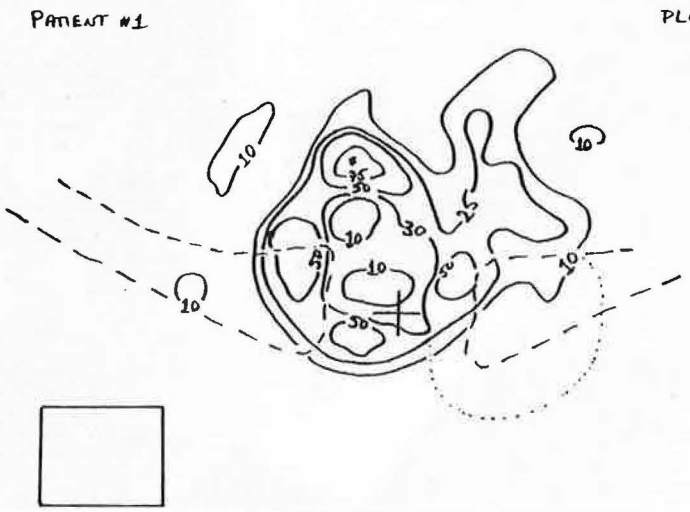

(b)

Figure 6

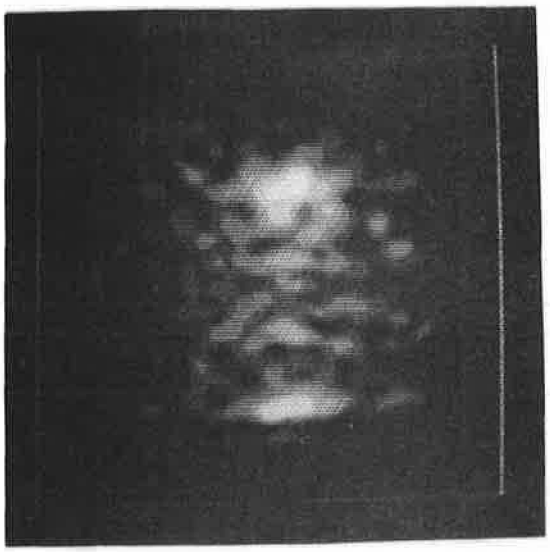

(a)

(b)

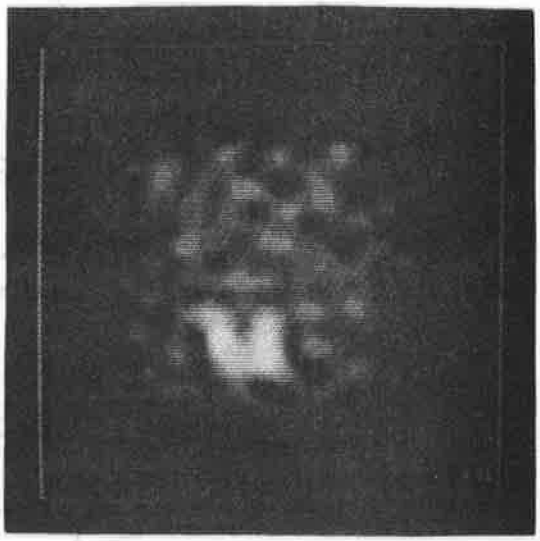

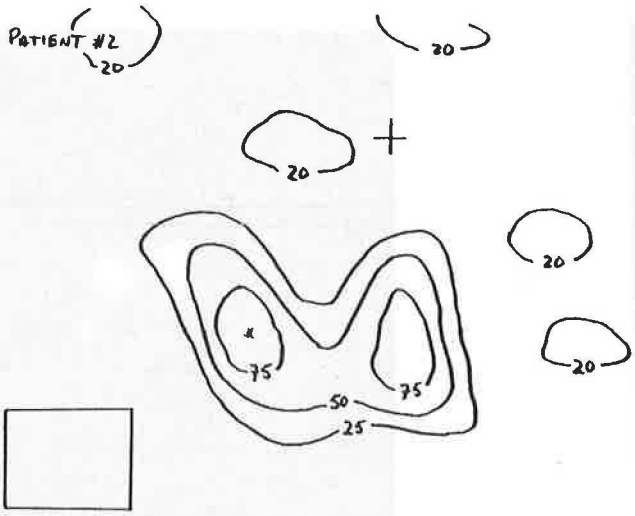

PLANE 5

(c)

Figure 7

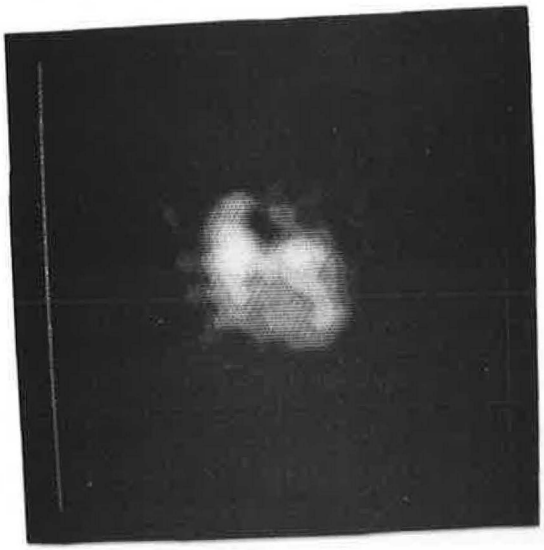

(a)

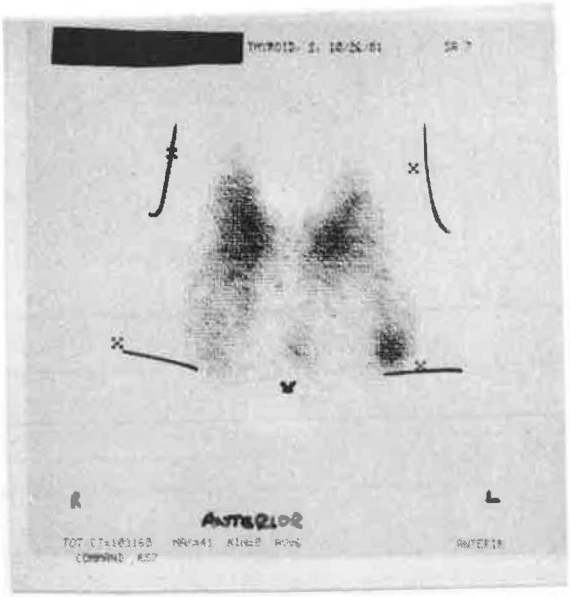

(b)

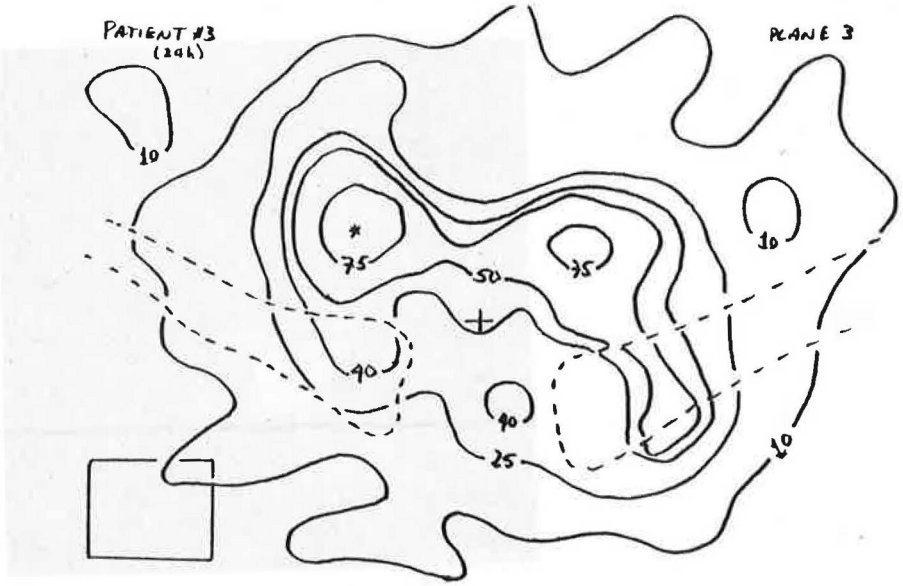

(c)

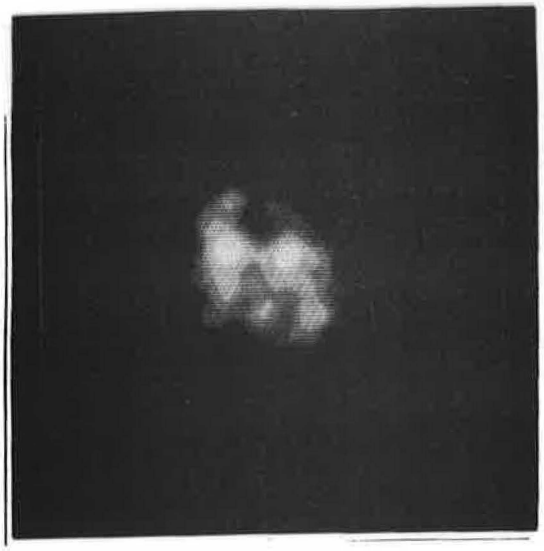

(d)

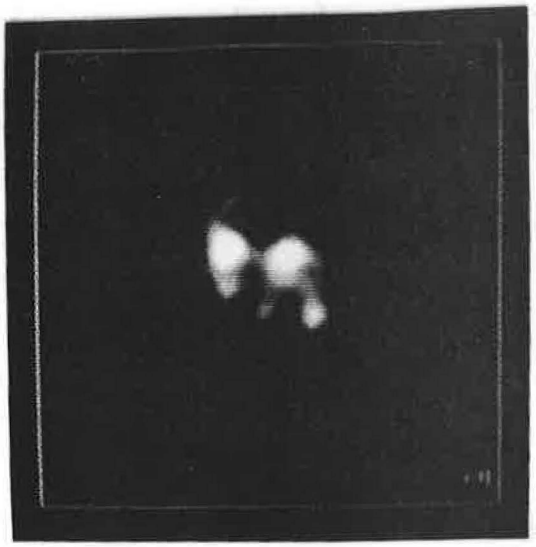

(e)

Figure 8

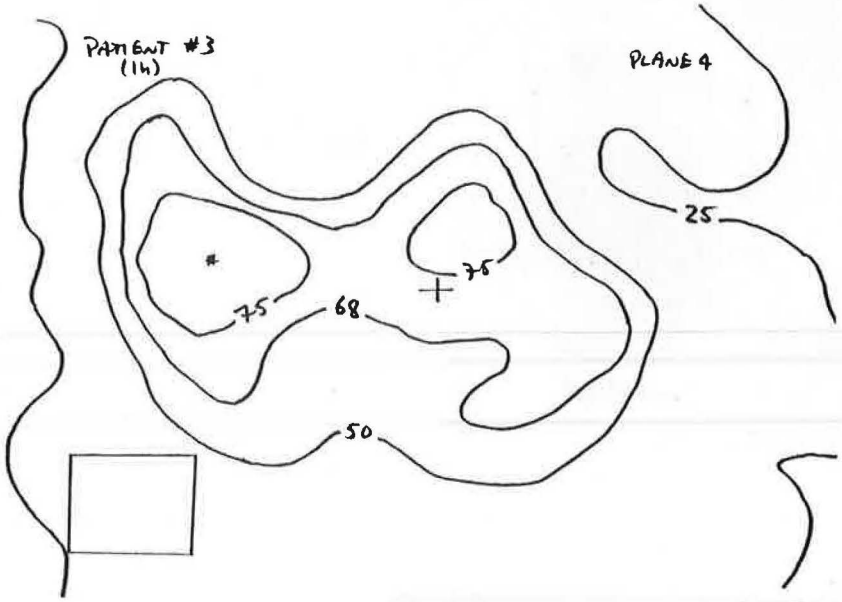
PATIENT #3
(1h)
PLANE 4
25
75
75
68
50

(a)

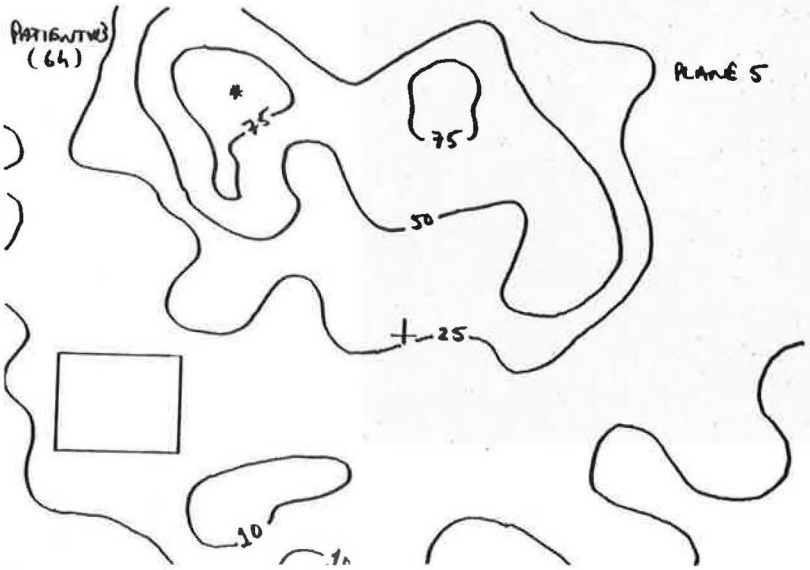
PATIENT #3
(6h)
PLANE 5
75
75
50
25
10

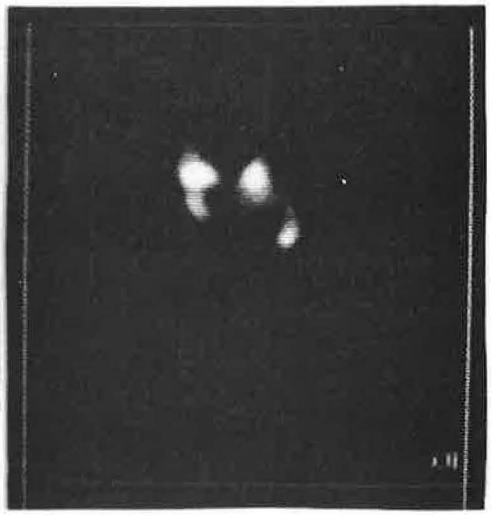

(b)

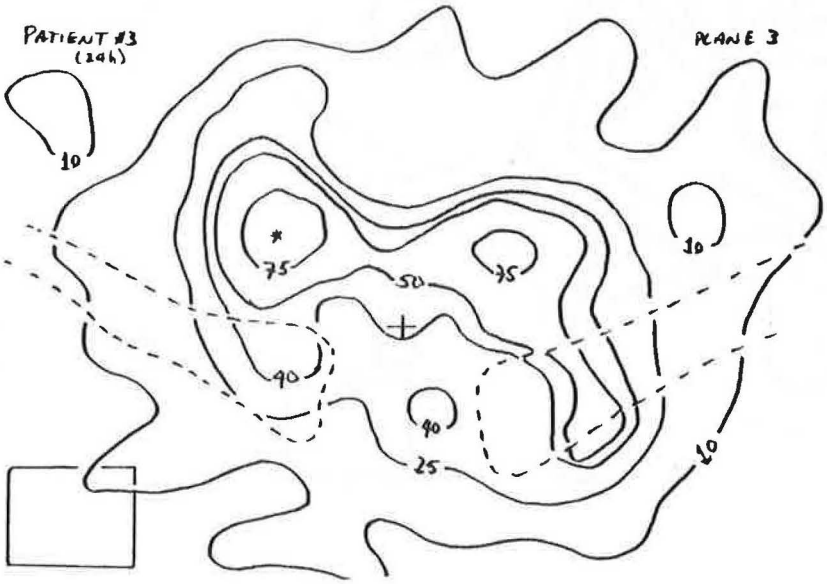
PATIENT #3
(24h)
PLANE 3
10
75
50
75
10
40
40
25
10

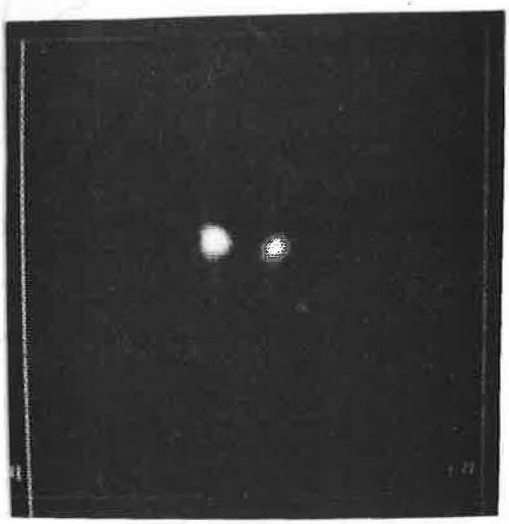

(c)

Figure 9

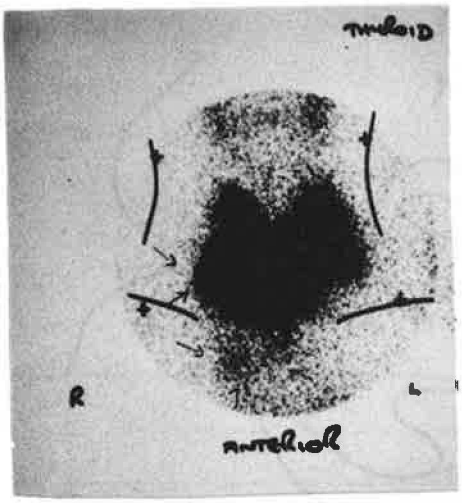

(a)

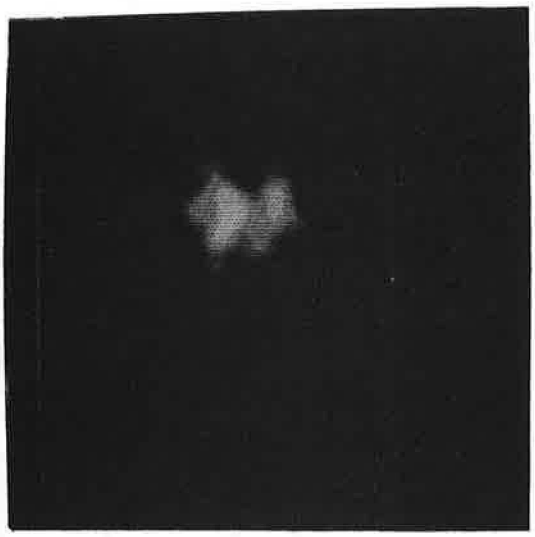

(b)

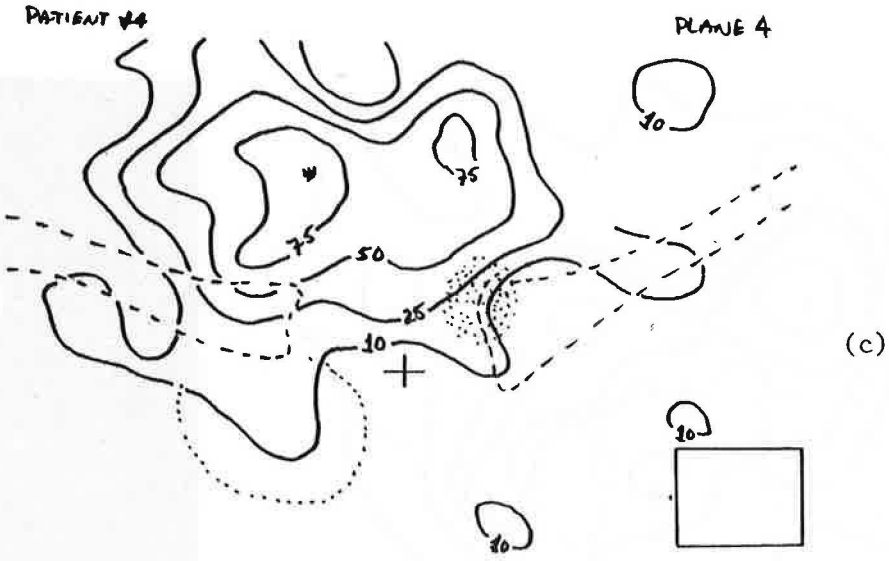

(c)

Figure 10

PATIENT #5

PLANE 2

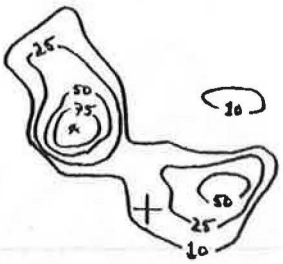

(a)

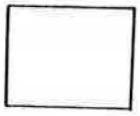

(b)

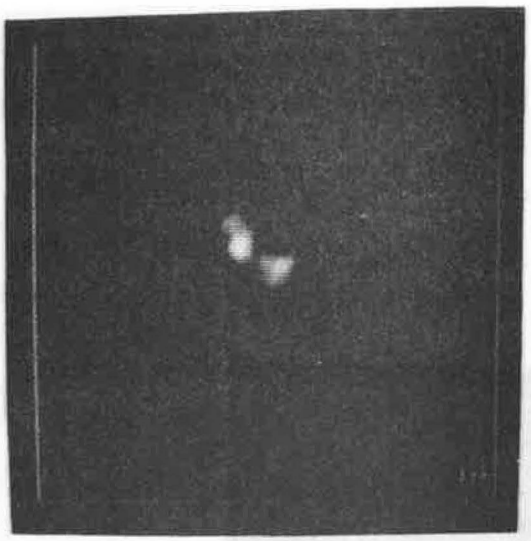

(c)

Figure 11

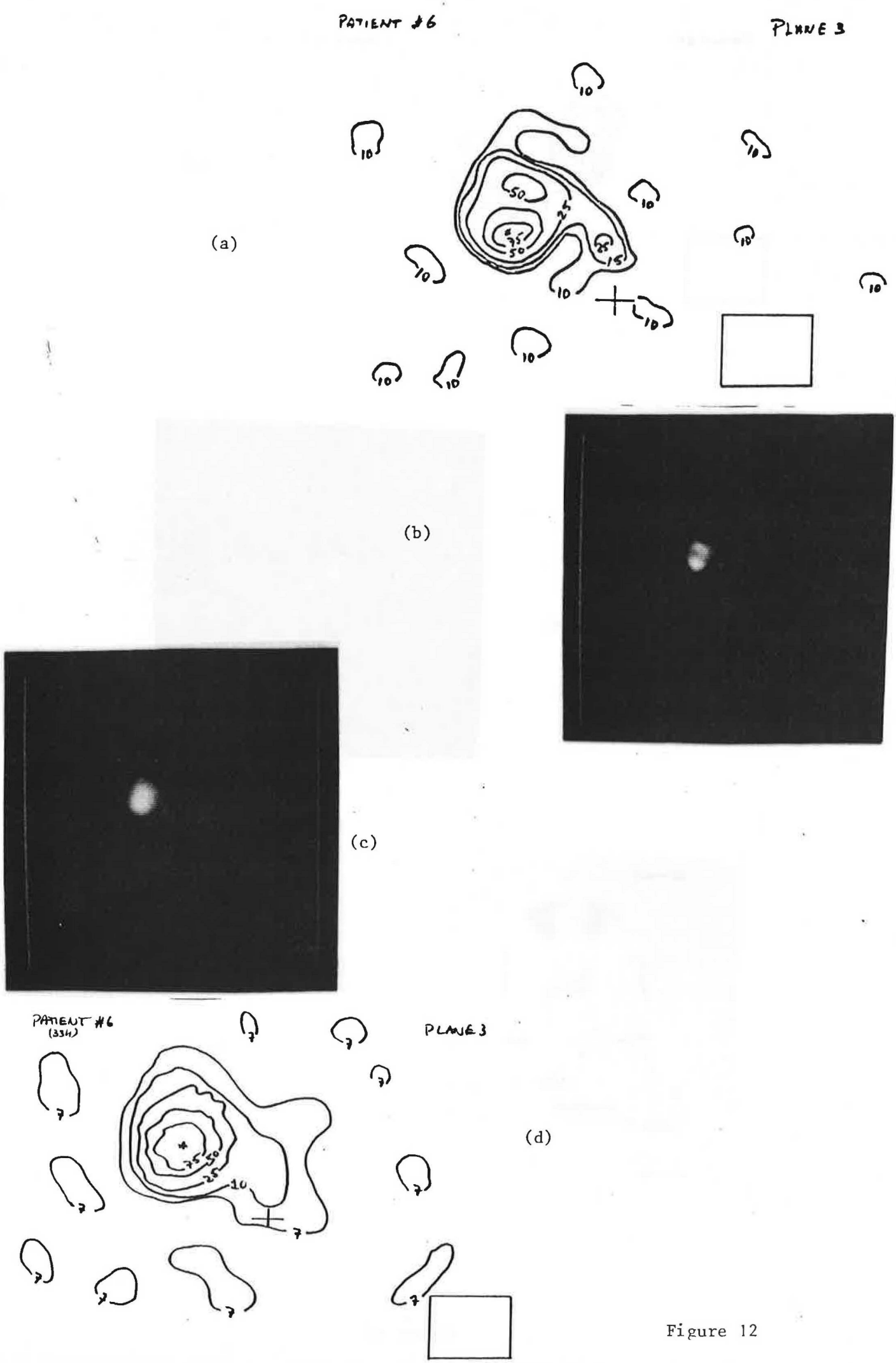
PATIENT #6
PLANE 3
(a)
10
50
25
75
15
(b)
(c)
PATIENT #6
(334)
PLANE 3
(d)
7
4
75
50
25
10

Figure 12

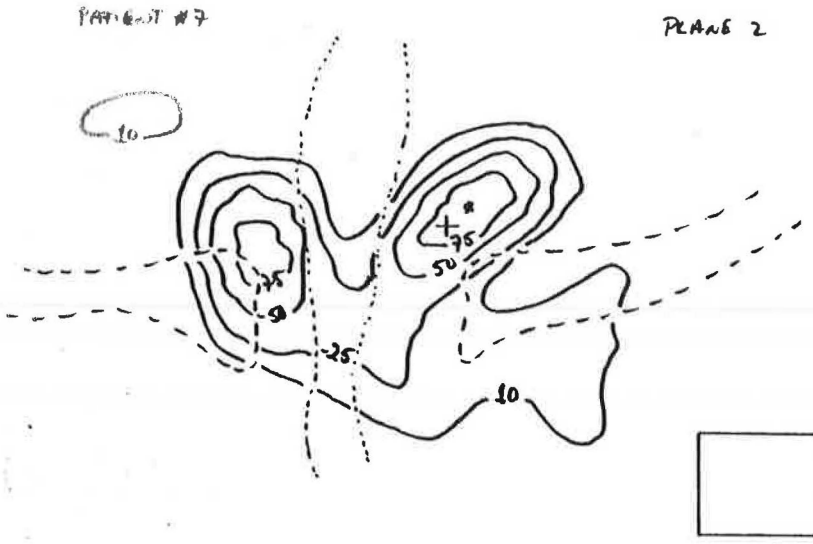

(a)

(b)

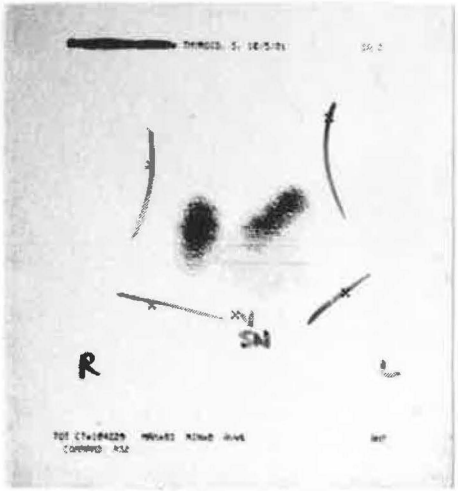

(c)

Figure 13